

Nanoscale Mechanical Characterization of Polymeric Fibers

J. CAYER-BARRIOZ,¹ A. TONCK,¹ D. MAZUYER,¹ PH. KAPSA,¹ A. CHATEAUMINOIS²

¹Laboratoire de Tribologie et de Dynamique des Systèmes, UMR 5513, ENISE, Ecole Centrale de Lyon, 36 avenue Guy de Collongue, 69130 Ecully, France

²Laboratoire de Physico-Chimie des Polymères et des Milieux Dispersés, UMR 7615, ESPCI, 10 rue Vauquelin, 75231 Paris, France

Received 11 June 2004; revised 13 September 2004; accepted 14 October 2004

DOI: 10.1002/polb.20323

Published online in Wiley InterScience (www.interscience.wiley.com).

ABSTRACT: The mechanical and viscoelastic behaviors of polymeric fibers varying in molecular weight have been determined at the nanometer scale with a surface force apparatus. The existence of a skin–core structure resulting from the elaboration process is pointed out. The role of fiber anisotropy is also discussed. © 2004 Wiley Periodicals, Inc. *J Polym Sci Part B: Polym Phys* 43: 264–275, 2005

Keywords: mechanical anisotropy; molecular weight; nanoindentation; polyamides; viscoelastic properties; mechanical properties

INTRODUCTION

In many applications involving textile structures (e.g., carpets, article felts, etc.), the abrasive wear resistance of the individual fibers is an important property. Within the context of textiles with improved tribological properties, poly(amide) fibers have emerged as an interesting alternative to natural fibers (such as wool or cotton) and other synthetic fibers (polypropylene, polyester, etc.). Analysis of the tribological behavior of such fibers requires, however, a better insight into their poorly understood structure and mechanical properties at the microscale, the latter being mainly controlled by the fiber forming process.¹ One of the most common manufacturing processes for synthetic fibers is based on melt spinning, followed by an additional hot drawing step to achieve the required high level of molecular orientation.² The latter is associated with the development of a microfibrillar structure that can be

described with different morphological models depending on the formation process.^{3,4} In one of the most popular descriptions, Prevorsek has assimilated the structure of oriented polyamide fibers to the so-called *Swiss-cheese* structure.³ In this model, the fibers are composed of a recurrent series of crystallites and amorphous domains called microfibrils, which are embedded in an oriented amorphous matrix, as illustrated in Figure 1. By virtue of this structural orientation, fiber mechanical properties are expected to present a strong anisotropy. Moreover, some core/skin effects can also be expected to take place as a result of the strong shear and thermal gradients involved in the melt spinning process. A detailed quantification of such anisotropic and potentially heterogeneous mechanical properties can, however, barely be achieved with bulk mechanical testing of the fibers.

In the past decade, many authors have demonstrated the potential of nanoindentation techniques for the measurement of the mechanical properties of polymer surfaces at the submicrometric scale.^{6–10} At this scale, the determination of mechanical properties from an indentation re-

Correspondence to: J. Cayer-Barrioz (E-mail: juliette.cayer-barrioz@ec-lyon.fr)

Journal of Polymer Science: Part B: Polymer Physics, Vol. 43, 264–275 (2005)
© 2004 Wiley Periodicals, Inc.

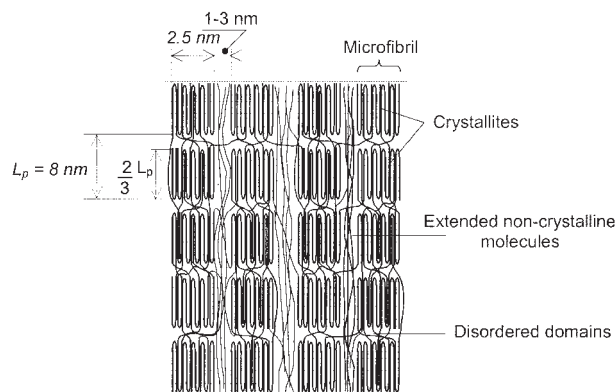


Figure 1. The Prevorsek's *Swiss-cheese* structural model of PA6 fibers [from ref. (3)]. The fiber axis is vertical. Crystallites are embedded in an amorphous oriented matrix and periodically organized to form microfibrils. The diameter of the microfibril, their periodic length, and the width of the amorphous disordered domains are taken from the literature⁴ and SAXS measurements.⁵

sponse faces many significant practical problems, such as the evaluation of the contact area and the inevitable existence of indenter tip imperfections.^{8,10} Additional difficulties also arise from the complex viscoelastoplastic response of polymeric materials.⁷ Despite these complexities, nanoindentation has, however, proven to be a powerful tool to evaluate the viscoelastic and plastic properties of polymers at the nanometer scale.

In this study, a method associating imaging procedures with nanoindentation experiments has been developed on the basis of a modified surface force apparatus. By means of a three-dimensional displacement modulation technique, the mechanical properties of the fiber in the radial and longitudinal directions have been continuously monitored during indentation. This technique was used to investigate the anisotropy of the fiber mechanical response as a function of the indentation depth. In addition, these measurements also provided some insight into the gradients of mechanical properties that resulted from skin/core effects.

EXPERIMENTAL

Materials

The polymeric fibers investigated in this study were purchased by Rhodia (Saint Fons, France).

The samples are made of thermoplastic semicrystalline poly(amide) 6 (PA6). They were enhanced by melt spinning followed by an additional hot drawing step² to reach a draw ratio of 3. The spinning speed was between 500 and 1200 m/min. The fibers presented a *Swiss-cheese* structure (Fig. 1). The average diameter of the fiber specimens was 42×10^{-6} m. Two kinds of fibers, differing in their molecular weight, were used and they will be denoted to as fiber A and B in the remainder of this article. Their number-average molecular weights, M_n , determined by size exclusion chromatography (SEC) in dichloromethane, were about 26 kg/mol for fiber A and 19 kg/mol for fiber B. The polydispersity index, I_p , was about 2, independent of the molecular weight (MW) (Table 1). The fiber glass-transition temperature (T_g), estimated by differential scanning calorimetry (DSC) at 1.6 K/s, is approximately 333 K when the fiber is dried and decreases to 258 K after soaking in water, because of plasticization effects.

2.2. Nanoindentation with a Surface Force Apparatus

Nanoindentation experiments were carried out on the Ecole Centrale de Lyon Surface Force Apparatus (SFA) that has been described in previous publications.¹¹⁻¹³ A diamond tip can be displaced with respect to a plane sample holder, in the three directions x , y (both parallel to the plane sample holder), and z (normal to the plane sample holder) with the expansion and the vibration of three piezoelectric actuators (Fig. 2). Three specific capacitive sensors were designed to measure relative displacements between the diamond tip and the sample holder in the three directions, with a resolution of 0.01 nm in each direction. Double cantilever sensors supporting the sample holder are used to measure the quasistatic normal and tangential forces (F_z and F_x , respectively). They are equipped with high resolution, highly compliant (up to 2×10^{-6} m/N), capacitive sensors for

Table 1. Main Characteristics of the Fibers: Diameter, ϕ , Molecular Weight, M_n , and Polydispersity Index, I_p

Fiber	A	B
ϕ (10^{-6} m)	42	42
M_n (kg/mol)	26	19
I_p	2	2

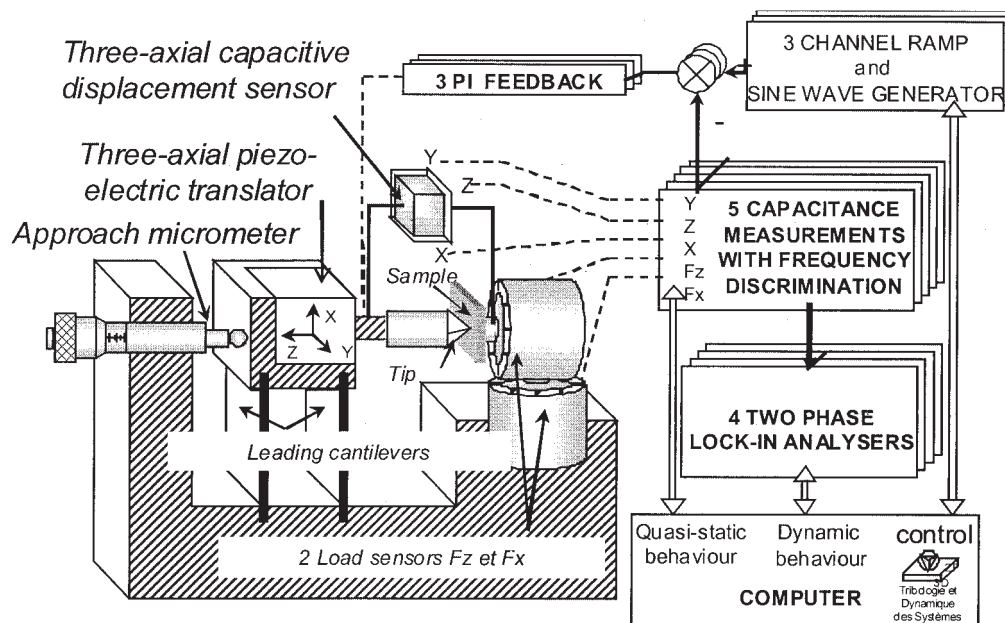


Figure 2. Schematic diagram of the SFA.¹¹

contact force measurements. Each sensor capacitance is determined by incorporating it in a liquid chromatography (LC) oscillator operated in the frequency range 5–12 MHz. Three closed feedback loops are used to control the high voltage amplifiers associated with the piezoelectric actuators. Two displacement closed feedback loops allow control of the tangential displacements x and y , whereas the operations in the normal direction z can be carried out either in displacement or normal force control.¹² Small amplitude (ca. 0.3 nm) oscillating displacements in the normal and tangential directions are superimposed on the quasistatic normal displacement in both the normal and tangential directions. The resulting modulated displacement and force signal are measured with double-phase synchronous analyzers that provide the in-phase and out-of-phase components of the normal and tangential mechanical transfer functions of the contact. From the in-phase (out-of-phase, respectively) signals, the elastic (viscous, respectively) properties of the contact are derived.

With the z feedback control in the constant force mode, the surface topography can be imaged with a diamond tip before or after the indentation.

Experimental Methodology

Nanoindentation tests have been performed in the controlled displacement mode at room tem-

perature (r.t.). During loading and unloading, the indentation speed was set to 1 nm/s. Three nanoindentation tests were performed on each fiber to check the reproducibility of the measurements. To continuously monitor the anisotropic contact stiffness, two small amplitude sinusoidal displacement motions were superimposed on the quasistatic loading in the normal and tangential directions. The corresponding frequencies ranged from 0.3 to 200 Hz.

A trigonal diamond tip with an angle of 90° between edges was used as the indenter. The indented fiber was maintained along its longitudinal axis on a flat sample holder, by means of a carbon pellet. The tip must be accurately located at the top of the fiber because the indentation tests are carried out radially. In such a situation, the normal displacement axis, z , corresponds to the radial direction of the fiber and the tangential direction, x , is parallel to the fiber longitudinal axis. Figure 3 presents an image of the fiber surface after an indentation under 10^{-4} N. No significant pile-up is observed in the indented area.

A number of studies have demonstrated the strong sensitivity of the mechanical properties of poly(amide) materials to water diffusion.^{14–16} During water diffusion, the plasticization of the poly(amide) amorphous phase is known to induce a very substantial decrease in elastic and plastic properties by virtue of a shift of the glass transition below r.t. As a consequence, the environment must be accurately controlled when any mechan-

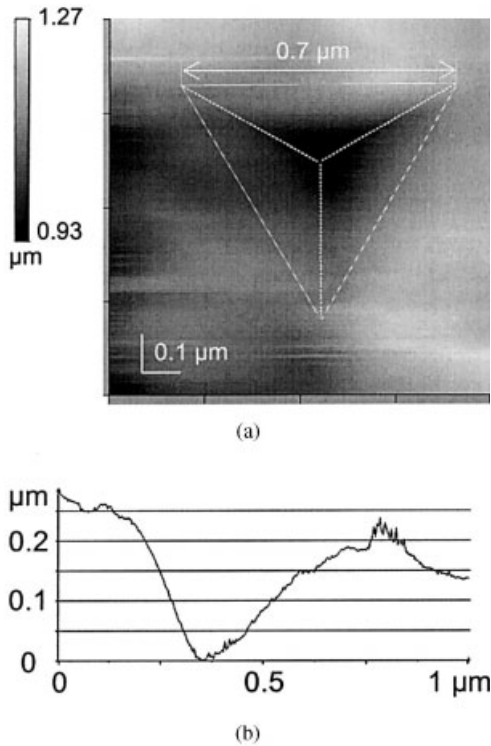


Figure 3. (a) Topographical image of the surface of fiber A after an indentation experiment performed at $100 \mu\text{N}$ and for a displacement speed of 1 nm/s , (b) Profile of the surface along the vertical axis. The profile does not show significant pile-up around the indent.

ical characterization is performed.¹⁴ To reduce the effects of variable moisture on poly(amide), the fibers were first dried for 12 h *in vacuo* at 10^{-9} bar and then exposed to nitrogen at 1 bar during the nanoindentation experiments.

RESULTS

Mechanical Anisotropy

The radial and tangential stiffnesses have been measured with fibers A during nanoindentation at a 10^{-4} N maximum load and a tip displacement rate of 1 nm/s . The modulation frequencies used for the stiffness measurement were set to 37 Hz in the radial direction and to 70 Hz in the tangential direction to avoid any disturbance caused by the system resonance. The changes in the in-phase stiffnesses, K_x and K_z , (in the tangential and the radial directions, respectively) as a function of the penetration depth are presented in Figure 4. As a first-order approximation, it can be assumed that the measured in-phase stiffness in a given direction is proportional to the contact area and to the material reduced modulus along that direction. Accordingly, the ratio of the normal to the tangential stiffness should be constant during the indentation of homogeneous isotropic materials. In Figure 4, it can, however, be seen that the ratio K_x/K_z is increasing as a function of the indenta-

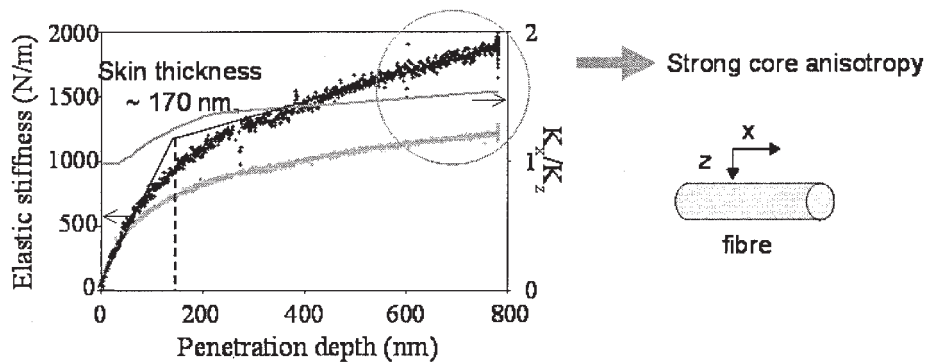


Figure 4. Changes in the elastic stiffness in the radial and tangential directions as a function of the penetration depth (indentation at 1 nm/s and at a maximum load of 10^{-4} N). The radial (tangential, respectively) modulation frequency used for the stiffness measurement was set to 37 Hz (70 Hz , respectively). The ratio of the tangential to the radial stiffness is also presented as a continuous grey line. The curve shows the increase in the fiber anisotropy with the indentation depth. (grey-filled diamond) radial elastic stiffness, (black filled diamond) tangential elastic stiffness. The thickness of the skin layer is estimated from the intercept of the two linear $K(h)$ responses observed at low and high indentation depths that correspond to situations where the mechanical contribution of the core and the skin, respectively, can be neglected.

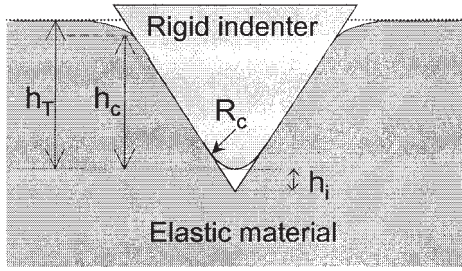


Figure 5. Schematic description of the indentation of an elastic half space by a rigid cone with a spherical tip. The total penetration depth is h , h_c is the plastic penetration, h_i is the tip defect, and R_c is the radius of curvature of the spherical tip. It can be seen that the elastic deflection of the surface around the contact is small compared to the total penetration depth.

tion depth. For low penetration depth, radial and tangential stiffnesses are similar. The deeper the penetration, the higher the difference between the elastic stiffnesses in the two directions. This result is indicative of the development of some anisotropy in the mechanical response of the fibers, because the penetration depth is increased. In addition to the anisotropic behavior, there is therefore also some evidence of a gradient of mechanical properties along the fiber radial direction. To investigate such an effect more closely, an attempt was made to assess the material reduced modulus and hardness as a function of the indentation depth.

According to Sneddon's analysis,¹⁷ the reduced modulus, E_z^* , and the hardness, H_z , along the radial direction can be estimated as follows:

$$E_z^* = \frac{\sqrt{\pi}}{2} \times \frac{K_z}{\sqrt{A}} \quad (1)$$

$$H_z = \frac{F_N}{A} \quad (2)$$

where K_z is the in-phase stiffness in the radial direction, F_N is the imposed load, and A is the projected contact area. The reduced modulus is defined as:

$$E_z^* = \frac{E_z}{1 - \nu^2} \quad (3)$$

where E_z is the Young's modulus in the radial direction and ν is the Poisson's ratio of the material.

These expressions were originally derived for homogeneous and isotropic material, which is clearly not the case of the studied polyamide fibers. In the absence of a well established contact theory dealing with anisotropic and heterogeneous materials, the above expressions will, however, be used as a first-order approximation of the material properties in the radial direction.

The determination of the contact area as a function of the indentation depth requires a precise calibration of the indenter geometry, especially close to the tip defect (Fig. 5).⁸ The calibration procedure employed consisted of indenting fused silica as a reference material. From the measurement of the elastic stiffness as a function of the penetration depth, an estimate of the radius of the tip defect is possible.¹⁸ In this investigation, the tip defect, h_i , was estimated to be about 16 nm.

To calculate the projected contact area, A , as a function of the indentation depth, the indenter was assimilated to an equivalent cone whose semiangle (i.e., 42°) was selected to give the same contact area as the indenter for a given penetration depth (Fig. 6).

Considering the 16 nm tip defect, h_i , and neglecting the effects of pile-up (that appeared negligible from topographical measurements in the indented area; see Fig. 3), the expressions for the reduced Young's modulus, E_z^* , and the hardness, H_z , in the radial direction become:

$$E_z^* = \frac{1}{2 \times \tan 42^\circ} \times \frac{K_z}{(h_c + h_i)} \quad (4)$$

$$H_z = \frac{1}{\pi \times (\tan 42^\circ)^2} \times \frac{F_N}{(h_c + h_i)^2} \quad (5)$$

where h_c is a plastic indentation depth. Within the context of elastoplastic indentation, this plastic depth can be estimated for any indentation

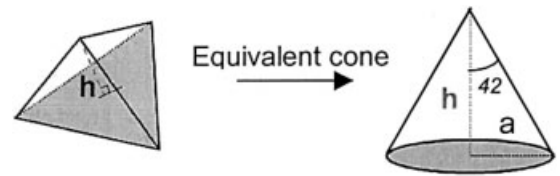


Figure 6. Definition of an equivalent cone with the same relationship between the projected contact area and the indentation depth as the used trigonal indenter.

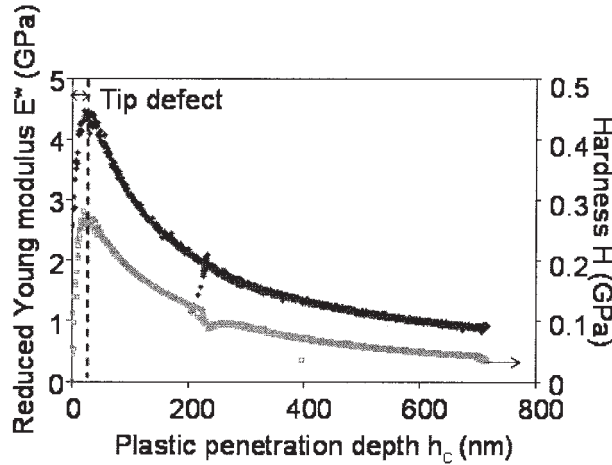


Figure 7. Changes in the reduced Young's modulus and the hardness as a function of the plastic penetration depth, h_c . The indentation was performed on fiber A at a 1 nm/s displacement rate and up to an indentation load of 10^{-4} N. (\diamond) Reduced Young's modulus, (\square) hardness.

depth, h , from a knowledge of the indentation load and the in-phase stiffness:⁹

$$h_c = h - \frac{F_N}{K_z} \quad (6)$$

In the above expression, the measured penetration depth, h , is thus assumed to be the sum of two separate contributions: the first one corresponds to the elastic deflection of the surface around the contact (as estimated from the ratio F_N/K_z), whereas the other component is the plastic indentation depth, h_c . Figure 7 illustrates the evolution of the calculated reduced Young's modulus, E_z^* , and hardness, H_z , as a function of the plastic penetration depth, h_c that were evaluated up to a maximum load of 10^{-4} N, for fiber A. The sharp increase in the calculated values at a low indentation depth (<20 nm) can be attributed to some insufficiencies in the tip defect correction and can therefore not be considered as a reliable measurement of the mechanical properties of the top surface layers. At a larger indentation depth, both the reduced modulus and the hardness seem to decrease as the plastic depth, h_c , increases. Three phenomena could account for such a decrease:

- (1) a substrate effect because of the finite dimensions of the fiber,
- (2) a strain rate effect because the indenta-

tion tests were carried out at an imposed displacement rate, \dot{h} , which means that the mean strain rate, $\dot{\epsilon}$, varied during the experiment according to the following relationship:^{19,20}

$$\dot{\epsilon} = \frac{\dot{h}}{h} \quad (7)$$

For the considered test conditions, the average strain rate was found to decrease from 0.05 s^{-1} to $1.25 \times 10^{-3} \text{ s}^{-1}$ when the indentation depth was increased from 0 to 800 nm,

- (3) a structural heterogeneity of the fiber, such as a skin–core effect.

Figure 3 shows that the dimension of the indented area is about 700 nm, which is largely inferior to the fiber diameter (42×10^{-6} m). Therefore, the indentation of a round cross-section fiber can be assimilated to that of a semi-infinite flat material. It can be concluded that the substrate effect is negligible. Nevertheless, this interpretation does not explain the specific decreasing shape of the curves.

To investigate the effects of strain rate on the indentation response, tests have been performed at different loading rates varying between 0.2 and 5 nm/s. These indentation rates were found to correspond to a mean strain rate, varying from $6 \times 10^{-4} \text{ s}^{-1}$ to $1 \times 10^{-3} \text{ s}^{-1}$ at 0.2 nm/s and from 0.02 s^{-1} to 0.25 s^{-1} at 5 nm/s. The resulting indentation responses were found to be essentially unaffected by the loading rate, which covered about three decades, that is, much more than the strain rate variation induced during a single indentation test at 1 nm/s. Accordingly, the observed decrease in the modulus and hardness as a function of the indentation depth cannot be attributed to the strain rate sensitivity of the fiber viscoplastic behavior. The existence of a skin–core effect resulting from the successive spinning processing steps and hot-drawing of the spun fibers² therefore remains the most probable explanation.

An estimate of the skin thickness can be deduced from the measured radial and tangential in-phase stiffness. In Figure 4, it can be seen that the changes in K_z and K_x as a function of the indentation depth are approximately linear within the limits of low (<100 nm) and high (>300 nm) displacements. According to eq 4, such

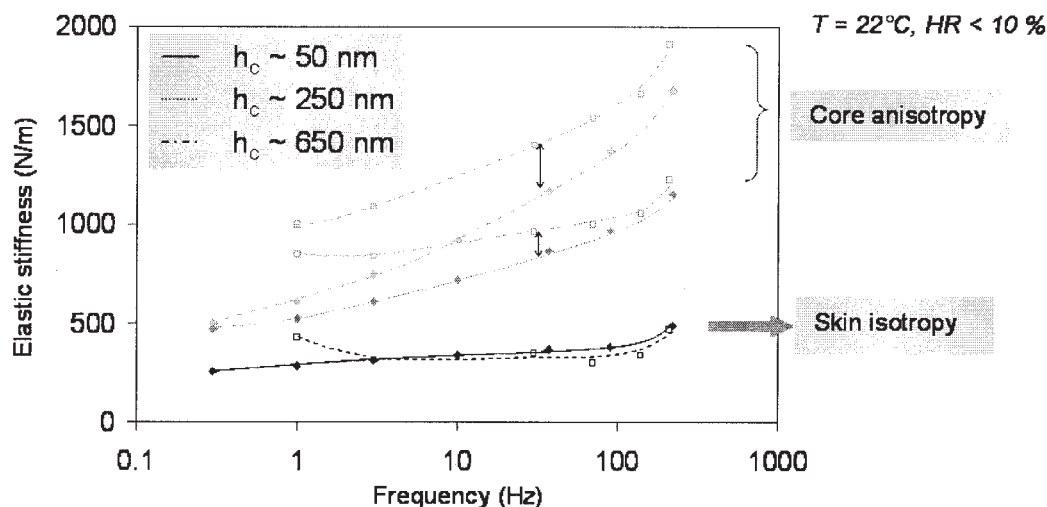


Figure 8. Effects of the displacement modulation frequency on the measured elastic properties of fiber A (displacement rate of 1 nm/s). The radial and tangential vibration frequencies are varied from 0.3 to 200 Hz. (\blacklozenge) Radial elastic stiffness, (\square) tangential stiffness. The penetration depth varies from 50 to 650 nm.

a linear relationship between the contact stiffness and the penetration depth can be considered as a signature of the indentation response of a homogeneous substrate if $h \sim h_c$. For low (high, respectively) indentation depths, one can therefore assume that the contributions of the core (the skin, respectively) to the measured response can be neglected. From the intercept of the two linear responses associated with low and high penetrations depths, respectively, the skin thickness can be estimated to be about 170 ± 30 nm for fiber A (see Fig. 4). Below 170 nm, the measured contact stiffness is not significantly affected by the mechanical response of the core, which means that the reduced modulus and hardness of the skin can be estimated with eqs 4 and 5. Similarly, the core properties can be calculated from the measured contact stiffness above 170 nm. From these calculations, the skin hardness in the radial direction was found to be about $250 \times 10^6 \text{ Pa} \pm 30 \times 10^6 \text{ Pa}$, that is, five times higher than the core hardness, whereas the skin Young's modulus ($4 \times 10^9 \text{ Pa} \pm 0.2 \times 10^9 \text{ Pa}$) is eight times greater than the core Young's modulus.

Fiber Viscoelastic Properties

The frequencies of the radial and tangential modulation signals have been varied between 0.3 and 200 Hz to investigate the viscoelastic response of the fibers. Figure 8 shows that the elastic stiffness in-

creases with frequency as a result of the fiber viscoelastic response. At a low penetration depth, radial and tangential elastic stiffnesses are nearly identical, independent of the frequency. When the indentation depth is increased within the core region, the anisotropy, as quantified by the difference between the radial and the tangential stiffnesses, is continuously increasing. The existence of an anisotropic core is thus confirmed within the whole investigated frequency range.

The viscoelastic losses in the radial and tangential directions may be compared in Figure 9 for a 250 nm penetration depth: the viscous dissipation, as quantified by the tangent of the phase angle, is higher in the radial direction than in the tangential direction, especially at low frequencies. This result has been obtained for a penetration depth higher than the estimated skin thickness. Hence, the core response significantly contributes to the measured stiffness. The mechanical anisotropy of the fiber therefore affects both the elastic and dissipative components of the viscoelastic behavior. An investigation of the radial viscous dissipation was also carried out at a deeper penetration: the viscous contributions increased with the penetration depth. It may be concluded that the core is more viscous than the skin.

Influence of the Fiber MW

The role of the polymer MW on the viscoelastic behavior of the fiber has been investi-

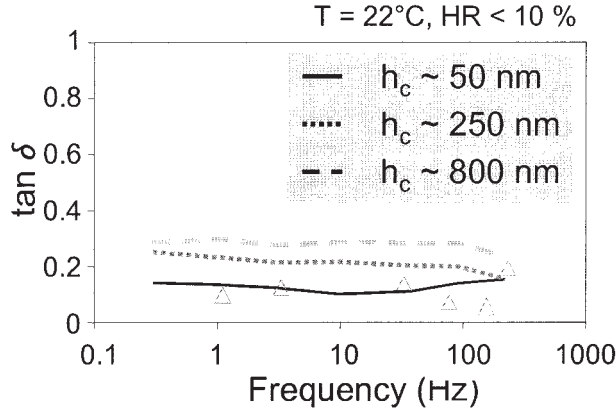


Figure 9. Influence of the displacement modulation frequency on the tangent of the loss angle measured in the radial and tangential directions during the indentation of fiber A at 1 nm/s. (—) $\tan \delta$ was measured in the radial direction for three penetration depths varying from 50 to 800 nm, (Δ) $\tan \delta$ in the tangential direction was measured at 250 nm penetration depth only.

gated. Dynamic nanoindentation tests have been carried out with the low M_n fibers, following the experimental methodology described in the section on experimental methodology. At a 10^{-4} N load, the measured penetration depth increases for a higher M_n . The fiber structure, as sensed by nanoindentation, is similar in both cases and also presents a skin–core effect. The skin thickness is about 220 nm for the low M_n fiber, instead of 170 nm for fiber A. These 50 nm differences could, however, result from some heterogeneity in the skin thickness (Fig. 10) and do not necessarily represent a significant MW effect. To consider the slight differences between the skin thicknesses of the various specimens, the penetration depths were normalized with respect to the estimated skin thickness (170 nm for fiber A and 220 nm for fiber B, respectively). For comparative purposes, the radial and tangential complex stiffnesses of both fibers have been reported in Figure 11 as a function of the normalized penetration depth. It can be seen that the skin viscoelastic properties

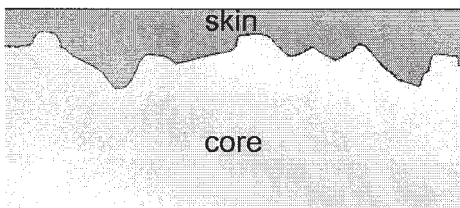


Figure 10. Geometric heterogeneity of the skin.

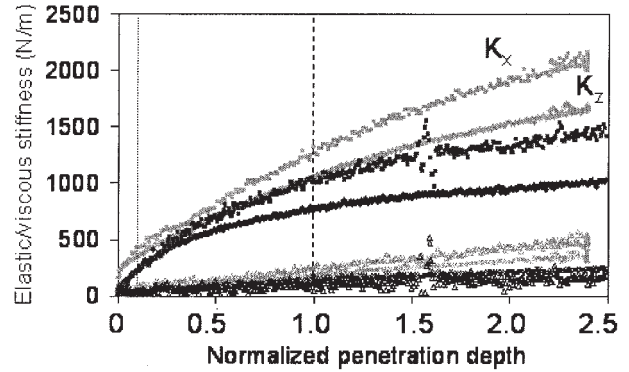


Figure 11. Changes in the in-phase and out-of-phase components of the contact stiffness as a function of the penetration depth for two fibers differing in their MW. The penetration depth has been normalized with respect to the skin thickness. (\blacklozenge) K_z , (\times) Im_z , (\square) K_x , (\triangle) Im_x . Black symbols correspond to fiber A ($M_n = 26$ kg/mol), grey symbols correspond to fiber B ($M_n = 19$ kg/mol).

are essentially independent of the MW. If the core structure (in terms of anisotropy) remains qualitatively unchanged, the corresponding viscoelastic properties in the radial and tangential directions are, however, strongly dependent on the fiber MW: the core properties for the low M_n fiber are two times higher than those of the high M_n fiber. Table 2 summarizes the viscoelastoplastic properties of the fibers A and B. Wide-angle X-ray scattering (WAXS) measurements showed that the crystallinity slightly increases (from 34 to 38%) as the M_n diminishes. Nevertheless, a 4% variation in crystallinity rate is not likely to result in a very significant modification of the elastoplastic response of the fiber. It may be supposed that the origin of these differences in the viscoelastic properties are because of some other parameters linked to the mechanical response of the amorphous phase.

The dissipative behavior of the low M_n fiber has also been characterized during dynamic nanoindentation. The trends formerly observed remain unchanged despite the modification of the MW: both radial and tangential stiffness increase with frequency. The differences between the radial and tangential stiffness strongly increases with penetration depth, which confirms the viscous anisotropy of the core. Figure 12 depicts a surprising feature of the frequency dependence of the tangent of the phase angle, $\tan \delta$: a damping peak is observed at about 30 Hz, but only in the tangential direction and independent of the con-

Table 2. Influence of the Molecular Weight on the Mechanical Structure and Elastoplastic Properties of the Fibers (Reduced Young's Modulus, E^* , and Hardness, H)

M_n (kg/mol)	19 (fiber B)	26 (fiber A)
Skin thickness (10^{-6} m)	0.22	0.17
Skin characteristics	$E \sim 4 \times 10^9$ Pa $H \sim 300 \times 10^6$ Pa	$E \sim 4 \times 10^9$ Pa $H \sim 250 \times 10^6$ Pa
Core characteristics	Strongly anisotropic $E'_{\text{tangential}} \sim 2.7 \times 10^9$ Pa $E'_{\text{radial}} \sim 1.8 \times 10^9$ Pa $E''_{\text{tangential}} \sim 0.9 \times 10^9$ Pa $E''_{\text{radial}} \sim 0.6 \times 10^9$ Pa $H \sim 100 \times 10^6$ Pa	Strongly anisotropic $E'_{\text{tangential}} \sim 1.2 \times 10^9$ Pa $E'_{\text{radial}} \sim 0.5 \times 10^9$ Pa $E''_{\text{tangential}} \sim 0.4 \times 10^9$ Pa $E''_{\text{radial}} \sim 0.4 \times 10^9$ Pa $H \sim 50 \times 10^6$ Pa

sidered penetration depths. The existence of this peak and its possible interpretation will be discussed later.

DISCUSSION

The above described experimental methodology allowed the mechanical characterization of PA6 fibers at the nanoscale. All the results tend to demonstrate the existence of a core–skin effect and to reveal the strong anisotropy induced by the fiber fibrillar structure. However, the low estimated value of the core radial Young's modulus ($\sim 0.5 \times 10^9$ Pa) may seem inconsistent with the bulk tensile modulus of the dry fiber in the glass-like state ($\sim 3 \times 10^9$ Pa). This low value might be explained by:

- (1) the existence of a humidity gradient within the fiber because of insufficient water desorption in the nanoindentation set-up,
- (2) a peculiar deformation behavior of the anisotropic skin–core system that is not properly taken into account in the indentation model used to assess modulus values.

The first hypothesis would lead to a system consisting of a plasticized poly(amide) core in a rubber-like state surrounded by a dry glassy skin. The boundary between the skin and the core would not be steep because water diffusion in polyamide is usually assumed to obey a Fickian model.¹⁶ Nevertheless, nanoindentation experiments indicate that, within the frame of the hypothesis of a water concentration gradient, dry skin would correspond to the first 200 nm in depth, whereas the plasticized core would represent the inner regions, deeper than 400 nm below the surface (as shown in Fig. 4). The measured elastoplastic properties of the core would therefore correspond to those of poly(amide) in a rubber-like state. At 295 K, the rubbery core ($T_g < 293$ K) and the glassy skin ($T_g = 333$ K) would be, respectively, located below and above the T_g (as schematically illustrated in Fig. 13). Because the humidity gradient is correlated to a value of the T_g , it should be possible to define a humidity gradient, that is, a penetration depth corresponding to a 295 K T_g . Figure 13 shows the correspondence between the T_g , the penetration depth, and the humidity gradient. A schematic profile of $\tan \delta$ can also be plotted versus the penetration depth. In such a configuration, a peak of $\tan \delta$ should be observed at a penetration depth inferior

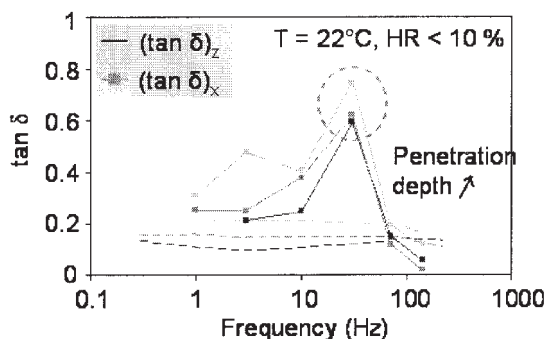


Figure 12. Tangent of the loss angle of the low M_n fiber B measured along the fiber radial and longitudinal directions for different frequencies and penetrations depths. The black line corresponds to a penetration depth of 50 nm, the middle grey line to 250 nm, and the pale grey line to 500 nm.

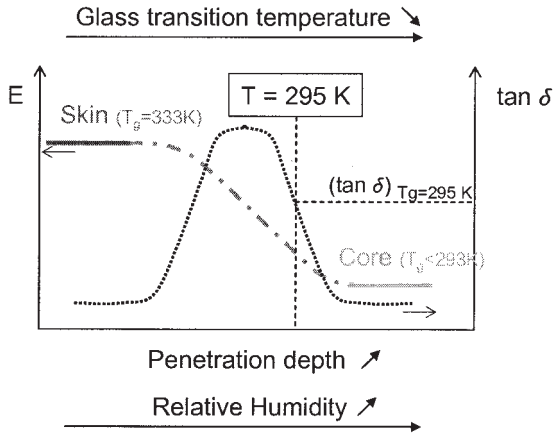


Figure 13. Schematic illustration of the influence of a gradient humidity on the evolution of viscoelastic behavior (Young's modulus and $\tan \delta$) of the fiber. A correlation can be made between the penetration depth, the humidity gradient and, therefore, the position of the T_g .

to 800 nm. At the same frequency, it may be supposed that:

$$(\tan \delta)_{T_g=333 \text{ K}} \leq (\tan \delta)_{T_g < 293 \text{ K}} \ll (\tan \delta)_{T_g=295 \text{ K}} \quad (8)$$

However, the frequency analysis of the viscous contributions (Figs. 9 and 12) in the radial direction reveals that $\tan \delta$ linearly increases with the penetration depth (or with the decreased T_g) to reach approximately 0.3 at the deepest penetration (the lowest T_g , respectively). This clearly demonstrates that the skin and the core are in an identical state. Moreover, some nanoindentation tests have been carried out on bulk poly(amide) 66 with a similar experimental methodology, in particular regarding material conditioning before testing. These tests unequivocally show that poly(amide) 66 is in a glass-like state (Young's modulus $E \sim 5 \times 10^9$ Pa), even for a 600 nm penetration depth. Because the water diffusion processes are similar for both poly(amide)s, these observations confirm the absence of a significant humidity gradient within the fiber.

The other hypothesis regarding the unexpected low value of the core modulus relies upon some specifics in the deformation behavior of the anisotropic skin–core system during indentation. The model that has been applied to estimate the fiber mechanical properties relies on the assumption of a homogeneous and isotropic material. The ob-

served linear dependence of the contact stiffness with the indentation depth within the skin zone and the core region tends to show that fiber anisotropy and heterogeneity does not induce a significant departure from the hypothesis of the model. In addition, good order of magnitude values of the moduli were derived. However, the fiber anisotropy could, for example, result in some errors in the estimate of the contact area, which could in turn induce some discrepancies in the determination of the modulus. In the absence of any reliable model for the elastoplastic indentation of anisotropic materials, it is difficult to assess the potential contribution of such effects.

Independent of the problem of the absolute moduli values, this investigation emphasizes the role of the MW on the mechanical properties of the fiber. When the MW decreases, the elastoplastic properties and the extent of crystallinity increase. Moreover, WAXS measurements show that the fiber microstructure and, more specifically, the characteristics of the oriented amorphous phase change with a decreasing MW:²¹ the lower the MW, the higher the orientation degree of the amorphous phase and the relative fraction of the oriented amorphous phase in the fiber. Consequently, a tentative description of the interrelationships between the mechanical properties and the orientation of the amorphous phase can be made. Figure 14 schematically depicts the structure of the fiber as a function of the MW and proposes a tentative description of the fiber deformation behavior. In the radial direction, the fiber can be mechanically modeled by three springs in series: K_1 represents the radial stiffness of the crystallites and K_2 (K_3 , respectively) corresponds to the stiffness of the oriented amorphous phase for the low-MW fiber (for the high-MW fiber, respectively). Therefore, the resulting stiffness in the radial direction may be expressed as:

$$\frac{1}{K_z} = \frac{1}{K_1} + \frac{1}{K_2} + \frac{1}{K_1},$$

for the fibre of low molecular weight (9)

$$\frac{1}{K_z} = \frac{1}{K_1} + \frac{1}{K_3} + \frac{1}{K_1},$$

for the fibre of high molecular weight (10)

Since $K_2 > K_3$ because of the extent of orientation of the amorphous phase,

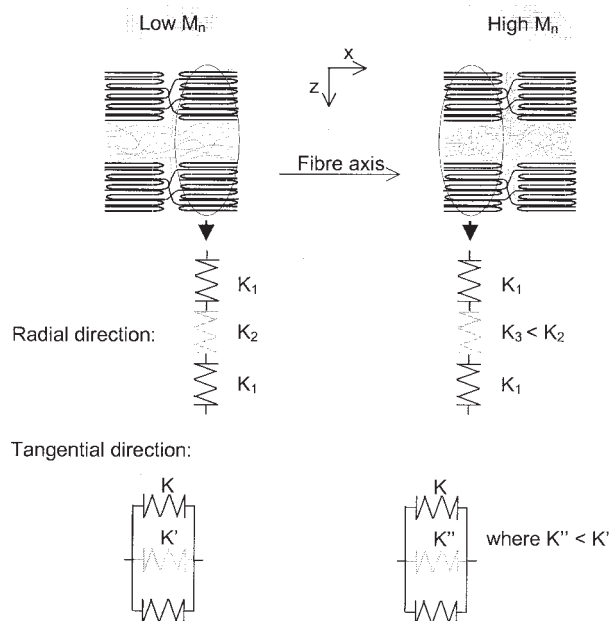


Figure 14. Schematic mechanical modeling of the fiber response in the radial and tangential directions as a function of the MW of the polymer. The stiffness of the crystallites is represented by K_1 in the radial direction (K in the tangential direction). The stiffness of the oriented amorphous phase of the fiber having the lowest MW (the highest, respectively) is K_2 (K_3 , respectively) in the radial direction and K' (K'' , respectively) in the tangential direction.

$$K_z(\text{low } M_n) > K_z(\text{high } M_n) \quad (11)$$

In the tangential direction, a similar approach can be made with three springs in parallel. K represents the tangential stiffness of the crystallites, K' (K'' , respectively) corresponds to the stiffness of the oriented amorphous phase of the fiber with the lowest MW (the highest, respectively) in the tangential direction. Because $K' > K''$,

$$\begin{aligned} K_x(\text{low } M_n) &= K + K' + K'' > K_x(\text{high } M_n) \\ &= K + K'' + K \quad (12) \end{aligned}$$

From this figure, it can be deduced that the stiffness in both directions will be higher for the low-MW fiber. This figure describes the response of an elastically deformed fiber, although major viscoplastic deformation is induced during indentation that could in turn induce a modification of the microfibrillar structure via dislocation motions and fragmentation of the crystallites. However, it can be assumed that the amorphous matrix re-

mains on the whole oriented (showing a kind of memory effect). Therefore, the low-MW fiber will still present a higher extent of orientation within the amorphous phase.

The fiber anisotropy is once more pointed out in Figure 12. A peak has been observed in the tangential direction and for the low-MW fiber only. The presence of this peak may be interpreted in terms of:

- (1) a coupling between the mechanical behavior of the amorphous and crystalline phases,²² if the fiber is considered as a fibrillar nanocomposite. Some studies on macroscopic composite systems such as metal/polymer/metal sandwiches emphasize the potential contribution of mechanical coupling effects between the responses of the elastic and viscoelastic phases.²³ It was particularly shown that the damping peak corresponding to the main mechanical relaxation of the viscoelastic phase may be drastically shifted along the temperature axis because of such coupling effects. If it is assumed that the fiber behaves like a nanocomposite made out of essentially elastic microfibrils embedded within a viscous amorphous matrix, similar effects could take place and result in the observed, orientation-dependent, damping peak observed at 30 Hz. However, this hypothesis does not explain MW dependence.
- (2) some intrinsic anisotropic viscoelastic behavior of the amorphous phase. Chain mobility may depend on load orientation because the fiber structure is anisotropic. This would be related to the MW because of the extent of orientation of the amorphous phase.

CONCLUSIONS

An investigation of the mechanical behavior of PA6 fibers has been carried out at a nanometer scale with a modified SFA. From the simultaneous measurement of the contact stiffness along the radial and longitudinal directions of the fiber, it was possible to establish the existence of a skin-core structure and to reveal the mechanical anisotropy associated with the fiber microfibrillar structure. The heterogeneous fiber microstructure consisted of a strongly anisotropic and dissi-

pative core surrounded by a 0.2 μm -thick hard skin. It was concluded that polymer plasticization associated with a water concentration profile cannot account for such a skin-core effect, which is more likely to result from the strong thermomechanical gradients experienced during the fiber spinning process. A decrease in the MW of the fibers was found to result in a slight increase in the crystallinity but was associated with a significant augmentation of the core elastoplastic properties that was tentatively related to the extent of orientation within the amorphous phase.

Rhodia Technical Fibers is acknowledged for its financial support and for supplying the PA6 fibers. The authors wish to express their gratitude to Gilles Robert and Franck Bouquerel. Special thanks are also due to Jean-Luc Loubet for helpful discussions.

REFERENCES AND NOTES

- Mukhopadhyay, S. *Polym Eng Sci* 1994, 34, 371–376.
- Penning, J. P.; van Ruiten, J.; Brouwer, R.; Gabriëls, W. *Polymer* 2003, 44, 5869–5876.
- Bukosek, V.; Prevorsek, D. C. *Int J Polym Mater* 2000, 47, 569–592.
- Prevorsek, D. C.; Harget, P. J.; Sharma, R. K.; Reimschuessel, A. C. *J Macromol Sci Phys* 1973, 8, 127–156.
- Cayer-Barrioz, J. Ph.D. Thesis, Ecole Centrale de Lyon, Number 2003-32, 2003.
- Oliver, W. C.; Pharr, G. M. *J Mater Res* 1992, 7, 1564–1583.
- Loubet, J. L.; Oliver, W. C.; Lucas, B. N. *J Mater Res* 2000, 15, 1195–1198.
- Briscoe, B. J.; Sebastian, K. S.; Adams, M. J. *J Phys D: Appl Phys* 1994, 27, 1156–1162.
- Briscoe, B. J.; Fiori, L.; Pelillo, E. *J Phys D: Appl Phys* 1998, 31, 2395–2405.
- Bucaille, J. L.; Felder, E.; Hochstetter, G. *J Mater Sci* 2002, 37, 3999–4011.
- Tonck, A.; Bec, S.; Mazuyer, D.; Georges, J. M.; Lubrecht, A. A. *Proceedings of the Institution of Mechanical Engineers*, 1999; 213 Part J, pp 353–361.
- Bec, S.; Tonck, A.; Georges, J. M.; Georges, E.; Loubet, J. L. *Philos Mag A* 1996, 74, 1061–1072.
- Georges, J. M.; Tonck, A.; Poletti, S.; Yamaguchi, E. S.; Ryason, P. R. *Tribol Trans* 1998, 41, 543–553.
- Hernandez, R. J.; Gavara, R. *J Polym Sci Part B: Polym Phys* 1994, 32, 2367–2374.
- Stuart, B.; Briscoe, B. J.; *Polym Int* 1995, 38, 95–99.
- Valentin, D.; Paray, F.; Guetta, B. *J Mater Sci* 1987, 22, 46–56.
- Sneddon, I. N. *Int J Eng Sci* 1965, 3, 47–57.
- Odoni, L. Ph.D. Thesis, Ecole Centrale de Lyon, Number 99-17, 1999.
- Tabor, D. *Technology* 1970, 1, 145–179.
- Johnson, K. L. In *Contact Mechanics*; Cambridge University Press: Cambridge, 1985; Chapter 6, pp 171–178.
- Cayer-Barrioz, J.; Mazuyer, D.; Kapsa, Ph.; Chateauminos, A.; Robert, G. *Polymer* 2004, 45, 2729–2736.
- Ward, I. M. In *Mechanical Properties of Solid Polymers*; Wiley-Interscience: New York, 1990; Chapter 8, pp 189–193.
- Cuillery, P.; Gaertner, R.; Tatibouet, J.; Mantel, M. *J Appl Polym Sci* 1997, 65, 2493–2505.